Real-Time FPGA-Based Analytical Space Harmonic Model of Permanent Magnet Machines for Hardware-in-the-Loop Simulation

Nariman Roshandel Tavana and Venkata Dinavahi

Department of Electrical and Computer Engineering, University of Alberta, Edmonton, AB T6G 2R3, Canada

This paper presents a real-time analytical space harmonic model of permanent magnet synchronous machines with shaped poles. The goal of this configuration is to produce an air-gap flux density distribution as close to sinusoidal as possible to enhance the machine performance. The analytical model is derived to predict the magnetic fields and the machine behavior by solving Maxwell's equations and applying the superposition theorem. The digital hardware realization of the model is developed on the field-programmable gate arrays (FPGAs) in a paralleled and pipelined paradigm for an efficient hardware design. Such real-time emulation on FPGA can be used in the design procedure and the assessment of newly prototyped controllers and drive systems in the hardware-in-the-loop platform. In this paper, the analytical model of the machine is simulated in real time on 7.5 ns input FPGA clock cycles, and the achieved executive time is 1.8 μs. The captured real-time analytical results demonstrate the good accuracy of the emulator in comparison with the offline 2-D time-stepping transient finite-element solution obtained by JMAG software.

***Index Terms*— Analytical modeling, field-programmable gate arrays (FPGAs), finite-element method (FEM), permanent magnet linear synchronous motor (PMLSM), real-time systems.**

NOMENCLATURE

$\boldsymbol{J}_M$	Equivalent magnetization current vector.
$\boldsymbol{a}_y, \boldsymbol{a}_z$	Unit vectors in y-direction and z-direction.
H	Magnetic field intensity.
B	Magnetic field density.
F	Thrust force.
e	Induced electromotive force.
φ	Flux-linkage of a winding.
L	Motor width.
g	Mechanical air-gap length.
k_{wn}	Winding factor of nth harmonic.
p_f	Coil packing factor.
P	Number of pole pairs.
l_m	Magnet height.
l_w	Winding height.
w_m	Magnet width.
w_w	Winding width.
τ	Pole pitch.
τ_{wp}	Winding pitch.
J_0	Current density.
N	Number of PM segments.
B_r	Remanence.
$\boldsymbol{v}_{abc_s}$	Three-phase voltage supply.
$\boldsymbol{i}_{abc_s}$	Three-phase armature current.
$\boldsymbol{L}_{abc_s}$	Inductance matrix.
$\boldsymbol{r}_s$	Resistance matrix.
N_c	Number of turns in a coil.
ν_s	Synchronous speed.

Manuscript received November 19, 2014; revised January 22, 2015; accepted March 11, 2015. Date of publication March 16, 2015; date of current version July 20, 2015. Corresponding author: N. Roshandel Tavana (e-mail: roshande@ualberta.ca).

Color versions of one or more of the figures in this paper are available online at http://ieeexplore.ieee.org.

Digital Object Identifier 10.1109/TMAG.2015.2413376

I. INTRODUCTION

DUE to the advantages of high power density, high efficiency, and low maintenance costs, permanent magnet (PM) machines are widely used in industrial and domestic applications [1], [2]. The flux density distribution of PM poles plays a crucial role in the machine performance, since the average values of thrust or torque and their fluctuation especially depend on this distribution. Ideally, for optimal performance, the machine should have sinusoidal air-gap flux density distribution, sinusoidal current waveform, and quasi-sinusoidal distribution of stator conductors [3]. Therefore, different methodologies, such as magnet-arc-shaping technique [4]–[8], pulsewidth modulation (PWM) approach [9], [10], modular PM pole method [11], [12], trapezoidal or sine structure with third harmonic injection shaping technique [13], [14], and stair-step-shaped magnetic poles model [15], have been proposed in the literature for the shaping of PM poles to produce a sinusoidal magnetic field and to improve the machine efficiency.

A variety of methods have been employed to model the dynamic performance of PM machines with shaped magnetic poles. A lumped electric or magnetic equivalent circuit model is the fastest and the most common technique to predict machine behavior. However, they suffer from the model inaccuracy particularly when the flux paths are complex and flux leakages are significant [16]. Another candidate is numerical solution, such as the finite-element method (FEM). Although FEM offers highly accurate results with due accounting of all nonlinear phenomena and spatial effects, it remains computationally onerous and cannot be used for real-time prediction of machine behavior even with the aid of the powerful processors to accelerate computations.

To overcome the aforementioned problems, a 2-D analytical space harmonic solution is employed in this paper for

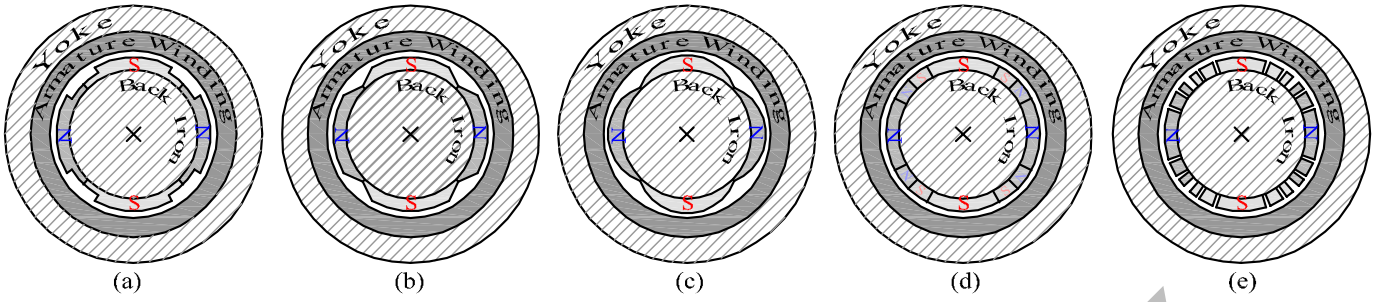

Fig. 1. PM machines with different pole shapes. (a) Stair-step shaping technique. (b) Trapezoidal or sine with third-harmonic injection method. (c) Arc-shaped model. (d) Modular magnetic poles. (e) PWM approach.

real-time simulation of PM machines with shaped magnetic poles with acceptable accuracy and reasonable computational efforts. The analytical approach offers the mathematical formulas for the prediction of machine performance as a function of machine geometry and design parameters, which would be very useful for real-time dynamic emulation, as well as design and performance optimization. Furthermore, the real-time emulation of the PM machine is carried out entirely in hardware on the field-programmable gate array (FPGA). FPGAs are now becoming the most preferred, reliable, and fastest computational engine for real-time simulation by offering many advantages, such as hardwired architecture, programmability with all the algorithms and functions, short development period, and full parallelism [17]–[20].

This paper presents a unified framework for the real-time FPGA-based analytical space harmonic model of PM machines with the shaped magnetic poles. Such a real-time analytical treatment is useful for the performance evaluation of the PM machines in the hardware-in-the-loop (HIL) configuration. HIL technology provides a cost- and time-effective approach in a virtual scenario for testing real devices in a nondestructive environment [21]–[26] and helps engineers to optimize the machine performance by running the emulated machine model in real-time using different geometrical parameters as many times as they need to reach the desired objectives.

This paper is organized as follows. Section II presents the analytical solution incorporating Maxwell's equations for dynamic simulation of PM machines; in addition, digital hardware realization of the proposed method on FPGA is described in this section. The close agreement between the FPGA-based real-time analytically predicted and finite-element calculated machine performances is demonstrated in Section III. Finally, the conclusions are given in Section IV.

II. Dynamic Analytical Space Harmonic Model of PM Machines With Shaped Magnetic Poles for Real-Time Simulation

A. Dynamic Performance of PM Machines

It is necessary to establish the voltage and torque equations of the PM machine that can describe its dynamic performance. Each variable in the governing equations of machine behavior, such as induced electromotive force (EMF) voltages, and inductance matrix is then determined by the analytical space harmonic model.

The three-phase voltage equations in the PM machine variables are given as

$$\boldsymbol{v}_{abc_s}(t) = \boldsymbol{r}_s \boldsymbol{i}_{abc_s}(t) + \boldsymbol{L}_{abc_s} \frac{d}{dt} \boldsymbol{i}_{abc_s}(t) + \boldsymbol{e}_{abc_s}(t). \quad (1)$$

Based on the instantaneous power of three-phase winding, the thrust/torque in a PM synchronous machine (PMSM) is obtained by

$$F(t) = \frac{1}{v_s} \boldsymbol{e}_{abc_s}(t) \cdot (\boldsymbol{i}_{abc_s}(t))^T. \quad (2)$$

For digital simulation of dynamic performance of PMSM, the differential equation (1) is discretized using forward Euler (FE) method as follows:

$$\boldsymbol{v}_{abc_s}(t) = \boldsymbol{r}_s \boldsymbol{i}_{abc_s}(t) + \frac{1}{\triangle t} \boldsymbol{L}_{abc_s} \boldsymbol{i}_{abc_s}(t) + \boldsymbol{e}_{abc_s}(t) + \boldsymbol{v}_{\text{hist}} \quad (3)$$

where $\triangle t$ is the simulation time-step size and $\boldsymbol{v}_{\text{hist}}$ is the history term in every time-step, given by

$$\boldsymbol{v}_{\text{hist}} = -\frac{1}{\triangle t} \boldsymbol{L}_{abc_s} \boldsymbol{i}_{abc_s}(t - \triangle t). \quad (4)$$

B. Magnet Shaping Methods in PM Machines

Since the structure of magnetic poles in the PM machine with arc, trapezoidal, PWM, modular, and stair-step shaping techniques, as shown in Fig. 1, is not uniform, solving the Maxwell's equations for the calculation of magnetic fields, and consequently the dynamic performance of the machine becomes more complex. The best way to establish analytical solution in these cases is to split magnetic poles to finitely many uniform and rectangular segments and then apply the layer method to each segment. In addition, as the soft magnetic parts are assumed to be infinitely permeable and all materials behave linearly in this layer approach, the resultant magnetic field can be obtained using the superposition theorem.

In this paper, the layer method is applied to a small segment of PM poles and the analytical prediction of magnetic field is presented thereafter. The governing equations can be used for all types of shaped PM poles in either rotary or linear structures. Without losing the generality of solution for the real-time analytical model of PM machines, a double-sided

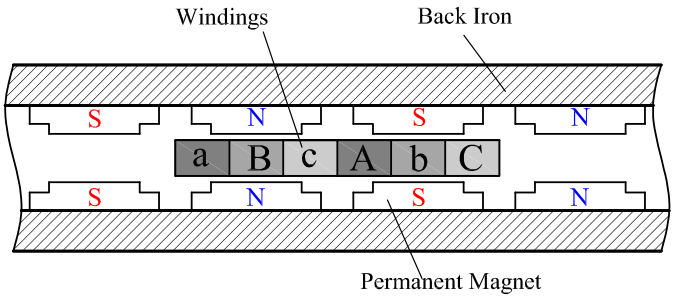

Fig. 2. Topology of a double-sided PMLSM with stair-step-shaped magnetic poles.

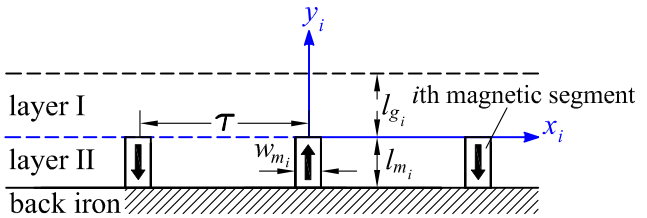

Fig. 3. Magnetic field layers for PMs.

air-core PM linear synchronous motor (PMLSM) with stair-step-shaped magnetic poles is chosen in this paper as the case study shown in Fig. 2.

C. Magnetic Field Distribution of PM Source

In order to provide analytical solution for the magnetic field distribution of ith magnetic segment of a shaped magnetic pole, the permeability of back iron is assumed to be equal to infinity. Consequently, Maxwell's equations lead to Laplace's and Poisson's equations in Layer I (airspace/winding layer) and Layer II (PM layer), respectively. Fig. 3 shows the field layers of the ith segment. The governing field equations in terms of magnetic vector potential can be expressed as follows [16], [27]:

$$\begin{cases} \nabla^2 \boldsymbol{A}_{I_i} = 0, & \text{in Layer I} \\ \nabla^2 \boldsymbol{A}_{II_i} = -\mu_0 \boldsymbol{J}_{M_i}, & \text{in Layer II} \end{cases} \tag{5}$$

where $\boldsymbol{J}_{M_i} = \nabla \times \boldsymbol{M}_i$ and $\boldsymbol{M}_i$ is the magnetization vector of the ith magnetic segment given by

$$\boldsymbol{M}_i = M_{y_i} \boldsymbol{a}_y \tag{6}$$

where M_{y_i} denotes the component of $\boldsymbol{M}_i$ in y-direction. The distribution of M_{y_i} can be expressed as the Fourier series

$$M_{y_i} = \sum_{n=1,3,\ldots}^{\infty} P_n \sin\left(\frac{m_n w_{m_i}}{2}\right) \cos\left(m_n x_i\right) \tag{7}$$

where $P_n = 4B_r/n\pi\mu_0$ and $m_n = n\pi/\tau$. The boundary conditions to be satisfied by the solution to (5) are

$$\begin{aligned} &H_{Ix_i}\big|_{y_i=l_{g_i}} = 0; \quad H_{IIx_i}\big|_{y_i=-l_{m_i}} = 0 \\ &H_{Ix_i}\big|_{y_i=0} = H_{IIx_i}\big|_{y_i=0}; \quad B_{Iy_i}\big|_{y_i=0} = B_{IIy_i}\big|_{y_i=0} \end{aligned} \tag{8}$$

where l_{g_i} is the effective air-gap length of the ith segment.

By solving (5), the flux density distribution produced by the ith segment in the air gap is provided from the curl of $\boldsymbol{A}_{I_i}$ as follows:

$$B_{Ix_i}(x_i, y_i) = \sum_{n=1,3,\ldots}^{\infty} m_n [a_{In_i} \exp(m_n y_i) - b_{In_i} \exp(-m_n y_i)] \sin(m_n x_i) \tag{9}$$

$$B_{Iy_i}(x_i, y_i) = -\sum_{n=1,3,\ldots}^{\infty} m_n [a_{In_i} \exp(m_n y_i) + b_{In_i} \exp(-m_n y_i)] \cos(m_n x_i) \tag{10}$$

where a_{In_i} and b_{In_i} are determined as

$$a_{In_i} = \exp(-2m_n l_{g_i}) b_{In_i} \tag{11}$$

$$b_{In_i} = -\frac{P_n \mu_0}{2m_n} \sin\left(\frac{m_n w_{m_i}}{2}\right) \frac{1 - \exp(-2m_n l_{m_i})}{1 - \exp(-2m_n (l_{m_i} + l_{g_i}))}. \tag{12}$$

Due to the linear behavior of the model, the total flux density of shaped PM poles is obtained using superposition theorem as

$$B_{Ix}(x, y) = \sum_{n=1}^{N} B_{Ix_i}(x_i, y_i); \quad B_{Iy}(x, y) = \sum_{n=1}^{N} B_{Iy_i}(x_i, y_i). \tag{13}$$

D. EMF Calculation

The total flux linkage of a distributed multicoil phase winding caused by the ith magnetic segments can be obtained as [28]

$$\begin{aligned} \varphi_i(x_i) &= \oint_s B_{Iy_i} \cdot ds = \int_0^L \int_{x_i - \tau_{wp}}^{x_i} B_{Iy_i} dx dz \\ &= \sum_{n=1,3,\ldots}^{\infty} \phi_{n_i} \cos m_n \left(x_i - \frac{\tau_{wp}}{2}\right) \end{aligned} \tag{14}$$

where

$$\begin{aligned} \phi_{n_i} = &\frac{8PLp_f k_{wn} N_c}{l_w} \sin\left(\frac{m_n \tau_{wp}}{2}\right) \\ &\times \int_{g_i}^{l_{g_i}} [a_{In_i} \exp(m_n y_i) + b_{In_i} \exp(-m_n y_i)] dy. \end{aligned} \tag{15}$$

Using Faraday's law, the induced EMF due to the ith segment is given by

$$\begin{aligned} e_i(x_i) &= -\frac{d\varphi_i}{dt} = -v_s \sum_{n=1,3,\ldots}^{\infty} \phi_{n_i} m_n \sin m_n \left(x_i - \frac{\tau_{wp}}{2}\right) \\ &= \sum_{n=1,3,\ldots}^{\infty} \text{CoEMF}_n \sin m_n \left(x_i - \frac{\tau_{wp}}{2}\right). \end{aligned} \tag{16}$$

Thus, the EMF produced by all magnetic segments can be expressed as follows:

$$e(x(t)) = \sum_{i=1}^{N} e_i(x_i). \tag{17}$$

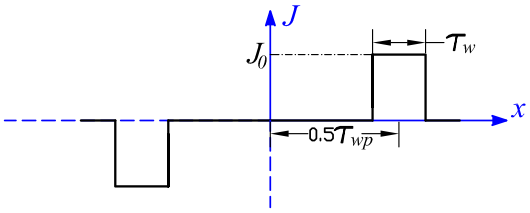

Fig. 4. Current distribution function of winding layer.

E. Armature Magnetic Field

The magnetic field caused by armature current is calculated in a similar way to the magnetic field of PM source. The governing equations in the winding layer and other regions are given by

$$\begin{cases} \nabla^2 \boldsymbol{A}_I = -\mu_0 \boldsymbol{J}_c, & \text{in Layer I} \\ \nabla^2 \boldsymbol{A}_{II} = 0, & \text{in Layer II.} \end{cases} \tag{18}$$

The current distribution function of winding layer $\boldsymbol{J}_c$, as shown in Fig. 4, is expanded as follows [28]:

$$\boldsymbol{J}_c = -\sum_{i=1,3,\ldots}^{\infty} J_n \sin(m_n x)\, \boldsymbol{a}_z \tag{19}$$

where

$$J_n = \frac{4J_0}{\tau m_n} \sin\left(m_n \frac{\tau_{wp}}{2}\right) \sin\left(m_n \frac{\tau_w}{2}\right). \tag{20}$$

The magnetic flux density distribution in the winding layer is obtained by

$$B_{Ix}(x,y) = \sum_{n=1,3,\ldots}^{\infty} m_n [a_{In} \exp(m_n y) - b_{In} \exp(-m_n y)] \times \sin(m_n x) \tag{21}$$

$$B_{Iy}(x,y) = -\sum_{n=1,3,\ldots}^{\infty} m_n \left[a_{In} \exp(m_n y) + b_{In} \exp(-m_n y) - \frac{\mu_0 J_n}{{m_n}^2}\right] \cos(m_n x) \tag{22}$$

where

$$a_{In} = \exp(2m_n l_w)\, b_{In} \tag{23}$$

$$b_{In} = \frac{\mu_0 J_n}{2{m_n}^2} \frac{\exp(2m_n(g+l_m)) - 1}{\exp(2m_n(g+l_m+l_w)) - 1}. \tag{24}$$

The boundary conditions are fulfilled as

$$H_{Ix}|_{y=-l_w} = 0; \quad H_{IIx}|_{y_i=g+l_m} = 0$$
$$H_{Ix}|_{y=0} = H_{IIx}|_{y=0}; \quad B_{Iy}\big|_{y=0} = B_{IIy}\big|_{y=0}. \tag{25}$$

F. Self and Mutual Inductances

The flux linkage of a phase winding due to the armature reaction field of another winding is expressed by

$$\varphi(x) = \oint_s B_{Iy} \cdot ds = \int_0^L \int_{x-\tau_{wp}/2}^{x+\tau_{wp}/2} B_{Iy}\, dx\, dz = \sum_{n=1,3,\ldots}^{\infty} \phi_n \cos m_n(x) \tag{26}$$

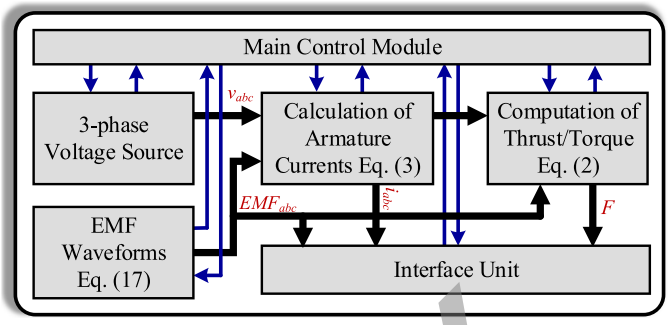

Fig. 5. Generic machine model implementation on FPGA.

where

$$\phi_n = \frac{8PLp_f k_{wn} N_c}{l_w} \sin\left(\frac{m_n \tau_{wp}}{2}\right) \times \int_0^{l_w} \left[a_{In} \exp(m_n y) + b_{In} \exp(-m_n y) - \frac{\mu_0 J_n}{{m_n}^2}\right] dy. \tag{27}$$

Thus, the self-inductance (L_s) and mutual inductance (L_m) of one slot per phase per pole armature winding can be calculated by

$$L_s = \frac{N_c \phi_a}{i_a}\bigg|_{i_b=i_c=0} = \frac{{N_c}^2 \varphi(0)}{J_0 \tau_w l_w} \tag{28}$$

$$L_m = \frac{N_c \phi_b}{i_a}\bigg|_{i_b=i_c=0} = \frac{{N_c}^2 \varphi(\tau_{wp})}{J_0 \tau_w l_w}. \tag{29}$$

G. Real-Time Hardware Emulation of Analytical Space Harmonic Model of PMSM on FPGA

The real-time emulation of PMLSM is carried out using the single precision floating-point number representation (IEEE standard 754). This 32 bit format enjoys the advantages of dynamic range, satisfactory accuracy, and acceptable computational time. A generic hardware realization of PM machine on FPGA is presented in Fig. 5. The hardware implementation of the machine performance at synchronous speed mainly consists of three states. The procedure starts with the calculation of three-phase voltage sources and the open-circuit voltages induced in the three-phase stator windings simultaneously in the first state. Then, in the second state, the stator current is computed by the history information (4) and FE integration technique. The instantaneous electromagnetic thrust/torque is obtained in the last state; meanwhile, the history terms are updated.

The hardware architecture of the machine model is realized by the aid of the source module for generating the three-phase voltage supply, matrix multiplication unit, dedicated floating-point multiply-add/subtract unit, and timer module for checking execution time constraint. All the aforementioned modules and their structures have been discussed in detail in [29] and [30]. However, the main and most complex hardware unit for the implementation of the analytical model of PMSM on FPGA is the EMF module where a Fourier series is designed and implemented. Fig. 6 shows the organization

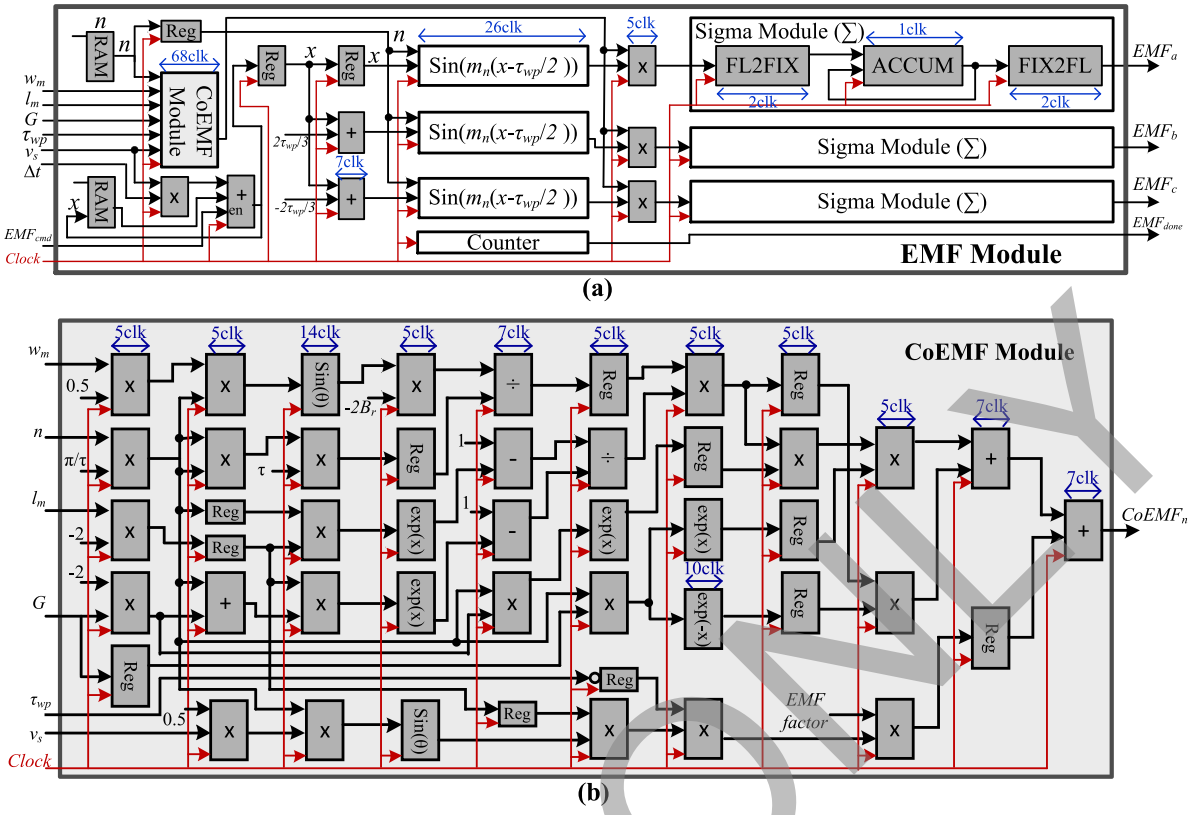

Fig. 6. Digital hardware realization of EMF module. (a) Deeply pipeline structure of EMF architecture. (b) Massively parallel implementation of EMF coefficient factor.

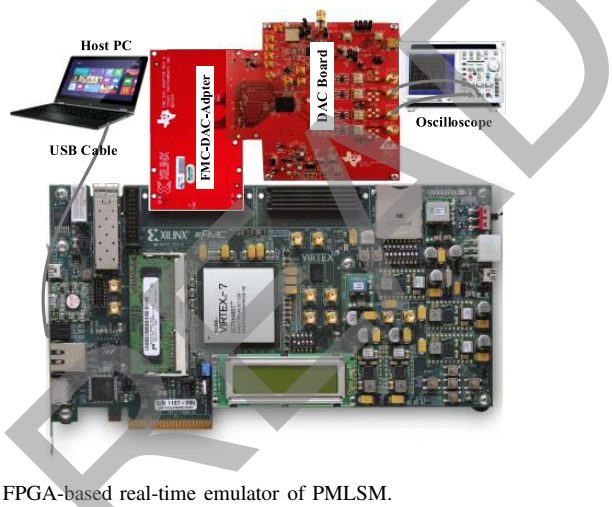

Fig. 7. FPGA-based real-time emulator of PMLSM.

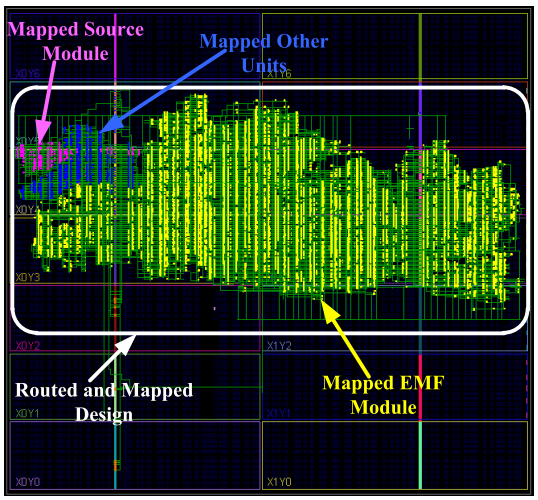

Fig. 8. Implemented design of PMLSM on the FPGA chip.

of the basic arithmetic operations and the storage elements for the realization of the EMF module. Fig. 6(a) shows how pipelining is employed to calculate EMF factors of 25 space harmonics. It can be observed in Fig. 6(b) that the sinusoidal and exponential functions as well as add, multiply, and divide operations are utilized to compute EMF (CoEMF) coefficient factor for each harmonic, and registers are inserted into data paths to synchronize data flow in the digital hardware design. The data march through the CoEMF submodule at every clock cycle and take the advantages of high computational data throughput.

In this architecture, the `Sigma` (∑) submodules, which are used to accumulate the harmonic contents of EMF waveforms, are arranged in a parallel scheme to compute induced open-circuit voltages of three-phase windings simultaneously. It should be noted that the accumulation in the `Sigma` submodule is carried out in the fixed-point format. The reason is that floating-point accumulator has a longer latency for high-frequency computation clock cycles and needs more logic resources to implement. The fixed-point accumulation

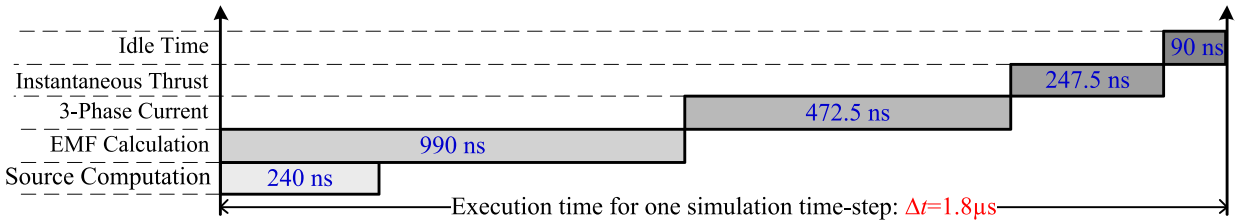

Fig. 9. Detailed execution time for one simulation time-step of emulated PMLSM.

TABLE I
HARDWARE RESOURCES CONSUMED FOR THE REAL-TIME ANALYTICAL EMULATION OF PMLSM

Real-Time Emulator	EMF Module	Source Module	Others	Total
Logic LUTs (303,600 available)	32,427 10.7%	778 0.3%	2,352 0.8%	35,557 11.7%
Memory LUTs (130,800 available)	1,310 1%	35 $\simeq$ 0%	179 0.1%	1524 1.2%
FFs (607,200 available)	24,882 4.1%	724 0.1%	2,570 0.4%	28,176 4.6%
Block RAMs (2,600 available)	163 7.9%	13 0.6%	2 0.1%	178 8.6%
DSP48 Blocks (2,800 available)	214 7.6%	6 0.2%	12 0.4%	232 8.3%

is in the format of 40.100 (1 sign bit, 39 integer, and 100 fractional bits) that can guarantee both the range and precision. In this structure, the input data are accumulated over each clock cycle and then converted to floating-point format. Therefore, the `Sigma` submodule contains one floating-to-fixed point converter, one fixed-point accumulator, and one fixed-to-floating point converter for the hardware realization [31].

III. FPGA-BASED REAL-TIME EMULATION AND FEM VALIDATION

A. Hardware Resource Utilization and Latencies

In this paper, the real-time analytical space harmonic model of the PMLSM is targeted to the Xilinx Virtex-7 development board, shown in Fig. 7. The FPGA XC7VX485T on this platform has 1955k logic cells, 68 Mb block RAM, 2800 DSP48E1, and 1200 I/O pins [32]. Fig. 8 presents the final hardware architecture implemented on the chip. It shows the compactness of the designed circuit for the digital hardware realization of PMSM, and also shows the distribution of each hardware unit on FPGA. The yellow, purple, and blue (light gray, gray, and dark gray in grayscale view) dots represent the area of the mapped design of the EMF module, the source module, and other units, respectively. Table I lists the resource utilization of FPGA-based real-time emulator. As can be seen in the table, the EMF module consumes more logic resources compared with other parts in the emulator. The full design consumes $\sim$12% and 8% of logic look-up tables (LUTs) and DSP48 blocks, respectively. Such resource conservation is a direct consequence of exploitation of deep pipelining in the EMF model computation.

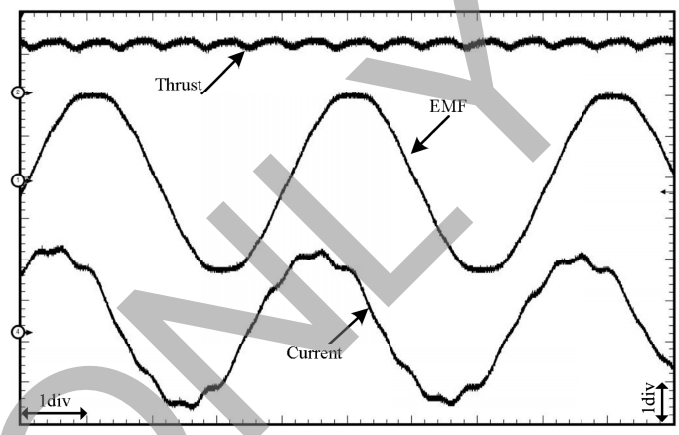

Fig. 10. Real-time oscilloscope traces of PMLSM performances at synchronous speed (time: 10 ms/div; thrust: 11 N/div; EMF: 14.2 V/div; current: 0.7 A/div).

According to the best case achievable FPGA clock frequency in the static timing analysis obtained at the end of the place and route process of hardware design, a clock frequency of 133.33 MHz was chosen for the implementation. Thus, the FPGA-based real-time emulation of the analytical model of PMLSM was executed within a time-step of 1.8 μs. The detailed execution time for one simulation time-step is shown in Fig. 9. It can be seen that the 90 ns idle time at the end of each time-step can be used for sending the real-time data out of the FPGA-based real-time emulator for external interfacing.

The real-time oscilloscope traces of the PMLSM behavior are shown in Fig. 10. The motor is fed with the three-phase voltage supply at synchronous speed. The thrust force, EMF, and current waveforms are shown in this figure, as will be explained in more detail in Section III-B.

B. Comparison Between the Real-Time Emulated and Finite-Element Calculated Machine Behavior

In this paper, finite-element analysis is employed to evaluate the performance of FPGA-based real-time emulated PMLSM.

Fig. 11 shows a graphical representation of finite-element predicted flux lines and flux density distribution of the analyzed machine, whose parameters and specifications are listed in the Appendix, in one pole pitch obtained from JMAG software. The execution time for running 80 ms (two cycles) of finite-element simulation even with time-step size of 50 μs for only half of one pole pitch of the PMLSM using the natural and antiperiodic boundary conditions with 5520 elements and 3052 nodes is 8 min and 22 s on a PC with

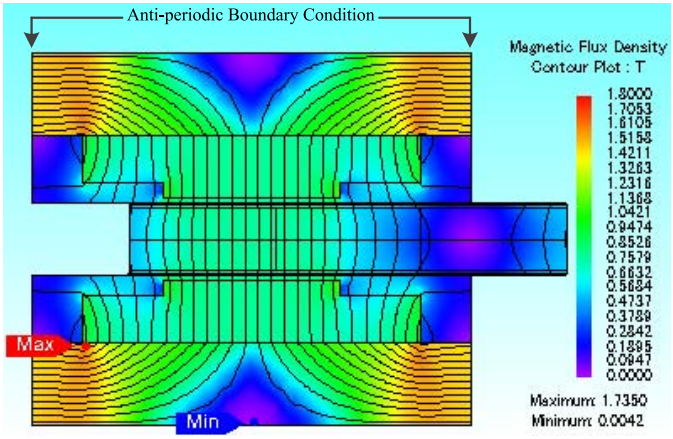

Fig. 11. Flux lines and flux density distribution in one pole pitch of the PMLSM with stair-step-shaped poles.

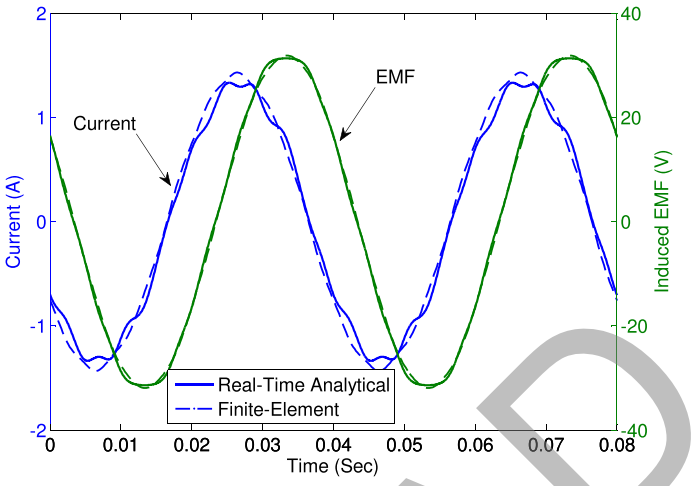

Fig. 12. Armature current and induced EMF waveform at synchronous speed.

Intel Core i7-2600 CPU at 3.4 GHz and 8 GB of installed memory (RAM), while the proposed analytical method was run in real time with a 1.8 μs time-step. Although real-time emulation is carried out in a shorter time-step size compared with finite-element analysis in this paper, it does not influence significantly on the differences between two sets of results.

In order to provide a detailed comparison, the real-time digital simulation data are exported from the FPGA using ChipScope analyzer and laid over the finite-element solutions.

Fig. 12 compares the real-time analytically and numerically predicted EMF waveforms of one phase of armature winding at a synchronous speed of 2.1 m/s. It can be seen that both sets of results agree quite well. A comparison of the FPGA-based real-time analytically predicted and finite-element calculated armature current resulting from the balanced three-phase sinusoidal voltage source is also presented in Fig. 12. A good agreement is again obtained in both the magnitude and wave shape. One reason for the slight discrepancy can be attributed to a finite and limited number of space harmonics (25 sine waves) that were computed and combined to represent the machine performance in the digital real-time emulation in this case. Moreover, the analytical model was

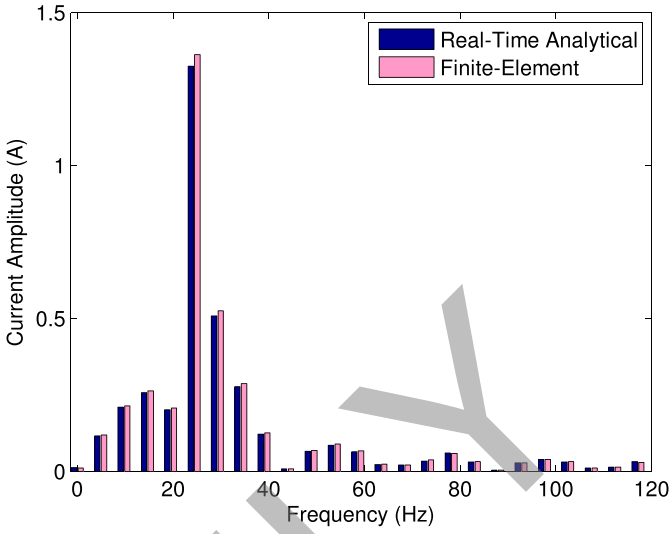

Fig. 13. Harmonic contents of the steady-state current.

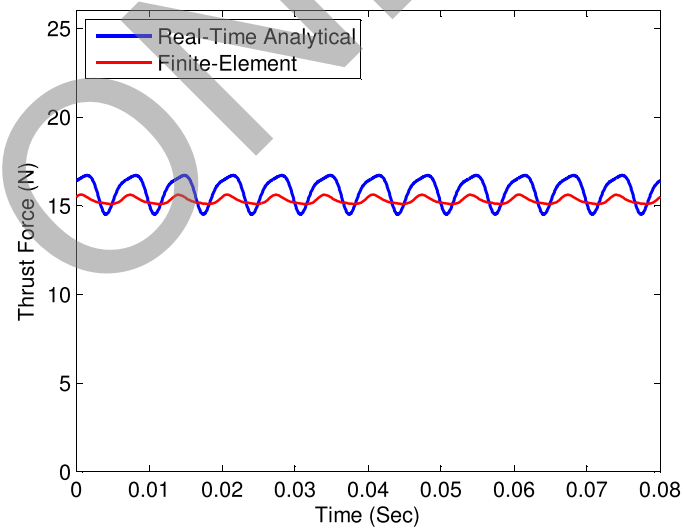

Fig. 14. Instantaneous thrust force at synchronous speed of PMLSM.

developed based on some simplifications such as ignoring the saturation effects in the iron cores and assuming a linear behavior for the machine model. The single-precision number calculation was used for hardware implementation due mainly to very fast computational requirement in real time, while double precision is employed in the finite-element analysis.

Fig. 13 shows the harmonic contents of the current waveform obtained from real-time analytical and finite-element model. It can be observed that there is close agreement between the results especially for the dominant harmonics.

Furthermore, the instantaneous thrust force waveform is presented in Fig. 14. The FPGA real-time emulated result tracks the FEM solution closely. The fluctuations in the real-time prediction are a consequence of the distortions on the analytically computed current waveform.

IV. Conclusion

Real-time digital emulators of electrical machines can play a key role in the industrial applications by enabling

TABLE II
PMLSM PARAMETERS

Parameter	Unit	Value	Parameter	Unit	Value
Pole pitch	mm	42	Higher magnet height	mm	5.9
Winding height	mm	6	Lower magnet height	mm	4.5
Winding width	mm	14	Higher magnet width	mm	17
Remanence	T	1.13	Lower magnet width	mm	7.7
Mech. air-gap	mm	1	Voltage supply	V	46.5

fast design optimization procedure and rapid testing of new technologies in drive systems in an HIL scenario. They must, however, be based on a detailed machine model simulated with significantly small time-step and capable of predicting the machine performances as a function of machine geometry. This paper proposes an FPGA-based real-time analytical space harmonic model of PM machines with shaped magnetic poles for HIL applications. Analytically derived formulas allow the prediction of machine performance in closed form as a function of physical dimensions and parameters of the machine. They facilitate the characterization of machine topologies, sensitivity analysis, iterative design optimization procedure, and real-time dynamic modeling of the machine. However, although finite-element analysis determines the magnetic field very precisely, because of saturation and so on, it remains time-consuming. Furthermore, while the presented case study in this paper addresses a linear PM machine, the model is significantly generalized for application to several types of rotary PM machines with shaped magnetic poles. All possible output variables of real-time emulated PMSM are presented and obtained by feeding the machine with the voltage sources similar to the real machine. Thus, the emulated PMSM can respond to any circumstances and changes that can be imposed by external devices and apparatus in the real-time HIL test. Taking advantages of the inherent parallel architecture of FPGA, the proposed hardware design is paralleled and pipelined to achieve an efficient FPGA implementation. FEM is then employed to evaluate the analytical solution of the machine model from the real-time emulator. The close agreement between real-time analytically calculated and numerically predicted machine performances confirms the effectiveness and accuracy of the proposed approach.

APPENDIX

Parameters and specifications of PMLSM with stair-step magnetic poles (see Table II).

ACKNOWLEDGMENT

This work was supported by the Natural Science and Engineering Research Council of Canada (NSERC).

REFERENCES

[1] Z. Q. Zhu and D. Howe, "Electrical machines and drives for electric, hybrid, and fuel cell vehicles," *Proc. IEEE*, vol. 95, no. 4, pp. 746–765, Apr. 2007.

[2] A. M. El-Refaie, "Motors/generators for traction/propulsion applications: A review," *IEEE Veh. Technol. Mag.*, vol. 8, no. 1, pp. 90–99, Mar. 2013.

[3] M.-F. Hsieh and Y.-S. Hsu, "An investigation on influence of magnet arc shaping upon back electromotive force waveforms for design of permanent-magnet brushless motors," *IEEE Trans. Magn.*, vol. 41, no. 10, pp. 3949–3951, Oct. 2005.

[4] Y. Li, J. Xing, T. Wang, and Y. Lu, "Programmable design of magnet shape for permanent-magnet synchronous motors with sinusoidal back EMF waveforms," *IEEE Trans. Magn.*, vol. 44, no. 9, pp. 2163–2167, Sep. 2008.

[5] Y. Li, J. Zou, and Y. Lu, "Optimum design of magnet shape in permanent-magnet synchronous motors," *IEEE Trans. Magn.*, vol. 39, no. 6, pp. 3523–3526, Nov. 2003.

[6] P. Zheng, J. Zhao, J. Han, J. Wang, Z. Yao, and R. Liu, "Optimization of the magnetic pole shape of a permanent-magnet synchronous motor," *IEEE Trans. Magn.*, vol. 43, no. 6, pp. 2531–2533, Jun. 2007.

[7] N. R. Tavana and A. Shoulaie, "Analysis and design of magnetic pole shape in linear permanent-magnet machine," *IEEE Trans. Magn.*, vol. 46, no. 4, pp. 1000–1006, Apr. 2010.

[8] M.-M. Koo, S.-M. Jang, Y.-S. Park, H.-I. Park, and J.-Y. Choi, "Characteristic analysis of direct-drive wind power generator considering permanent magnet shape and skew effects to reduce torque ripple based on analytical approach," *IEEE Trans. Magn.*, vol. 49, no. 7, pp. 3917–3920, Jul. 2013.

[9] S. Chaithongsuk, N. Takorabet, and F. Meibody-Tabar, "On the use of pulse width modulation method for the elimination of flux density harmonics in the air-gap of surface PM motors," *IEEE Trans. Magn.*, vol. 45, no. 3, pp. 1736–1739, Mar. 2009.

[10] A. H. Isfahani, "Analytical framework for thrust enhancement in permanent-magnet (PM) linear synchronous motors with segmented PM poles," *IEEE Trans. Magn.*, vol. 46, no. 4, pp. 1116–1122, Apr. 2010.

[11] A. H. Isfahani, S. Vaez-Zadeh, and M. Azizur Rahman, "Using modular poles for shape optimization of flux density distribution in permanent-magnet machines," *IEEE Trans. Magn.*, vol. 44, no. 8, pp. 2009–2015, Aug. 2008.

[12] L. Wu and Z.-Q. Zhu, "Analytical modeling of surface-mounted PM machines accounting for magnet shaping and varied magnet property distribution," *IEEE Trans. Magn.*, vol. 50, no. 7, pp. 1–11, Jul. 2014, Art. ID 8101511.

[13] S.-M. Jang, H.-I. Park, J.-Y. Choi, K.-J. Ko, and S.-H. Lee, "Magnet pole shape design of permanent magnet machine for minimization of torque ripple based on electromagnetic field theory," *IEEE Trans. Magn.*, vol. 47, no. 10, pp. 3586–3589, Oct. 2011.

[14] K. Wang, Z. Q. Zhu, and G. Ombach, "Torque enhancement of surface-mounted permanent magnet machine using third-order harmonic," *IEEE Trans. Magn.*, vol. 50, no. 3, pp. 735–747, Mar. 2014, Art. ID 8100210.

[15] N. R. Tavana, A. Shoulaie, and V. Dinavahi, "Analytical modeling and design optimization of linear synchronous motor with stair-step-shaped magnetic poles for electromagnetic launch applications," *IEEE Trans. Plasma Sci.*, vol. 40, no. 2, pp. 519–527, Feb. 2012.

[16] J. Wang, G. W. Jewell, and D. Howe, "A general framework for the analysis and design of tubular linear permanent magnet machines," *IEEE Trans. Magn.*, vol. 35, no. 3, pp. 1986–2000, May 1999.

[17] Y. El-Kurdi, D. Giannacopoulos, and W. J. Gross, "Hardware acceleration for finite-element electromagnetics: Efficient sparse matrix floating-point computations with FPGAs," *IEEE Trans. Magn.*, vol. 43, no. 4, pp. 1525–1528, Apr. 2007.

[18] W. Zhao, E. Belhaire, C. Chappert, and P. Mazoyer, "Power and area optimization for run-time reconfiguration system on programmable chip based on magnetic random access memory," *IEEE Trans. Magn.*, vol. 45, no. 2, pp. 776–780, Feb. 2009.

[19] Y. Cai, S. Jeon, K. Mai, and B. V. K. V. Kumar, "Highly parallel FPGA emulation for LDPC error floor characterization in perpendicular magnetic recording channel," *IEEE Trans. Magn.*, vol. 45, no. 10, pp. 3761–3764, Oct. 2009.

[20] Y. Chen and V. Dinavahi, "Multi-FPGA digital hardware design for detailed large-scale real-time electromagnetic transient simulation of power systems," *IET Generat., Transmiss. Distrib.*, vol. 7, no. 5, pp. 451–463, May 2013.

[21] C. Dufour and J. Belanger, "On the use of real-time simulation technology in smart grid research and development," *IEEE Trans. Ind. Appl.*, vol. 50, no. 6, pp. 3963–3970, Nov./Dec. 2014.

[22] D. N. Dyck, T. Rahman, and C. Dufour, "Internally consistent nonlinear behavioral model of a PM synchronous machine for hardware-in-the-loop simulation," *IEEE Trans. Magn.*, vol. 50, no. 2, pp. 853–856, Feb. 2014, Art. ID 7021104.

[23] M. Steurer, C. S. Edrington, M. Sloderbeck, W. Ren, and J. Langston, "A megawatt-scale power hardware-in-the-loop simulation setup for motor drives," *IEEE Trans. Ind. Electron.*, vol. 57, no. 4, pp. 1254–1260, Apr. 2010.

[24] W. Ren, M. Steurer, and T. L. Baldwin, "Improve the stability and the accuracy of power hardware-in-the-loop simulation by selecting appropriate interface algorithms," *IEEE Trans. Ind. Appl.*, vol. 44, no. 4, pp. 1286–1294, Jul./Aug. 2008.
[25] B. Lu, X. Wu, H. Figueroa, and A. Monti, "A low-cost real-time hardware-in-the-loop testing approach of power electronics controls," *IEEE Trans. Ind. Electron.*, vol. 54, no. 2, pp. 919–931, Apr. 2007.
[26] H. Li, M. Steurer, K. L. Shi, S. Woodruff, and D. Zhang, "Development of a unified design, test, and research platform for wind energy systems based on hardware-in-the-loop real-time simulation," *IEEE Trans. Ind. Electron.*, vol. 53, no. 4, pp. 1144–1151, Jun. 2006.
[27] S. Vaez-Zadeh and A. H. Isfahani, "Multiobjective design optimization of air-core linear permanent-magnet synchronous motors for improved thrust and low magnet consumption," *IEEE Trans. Magn.*, vol. 42, no. 3, pp. 446–452, Mar. 2006.
[28] J. Wang and D. Howe, "Design optimization of radially magnetized, iron-cored, tubular permanent-magnet machines and drive systems," *IEEE Trans. Magn.*, vol. 40, no. 5, pp. 3262–3277, Sep. 2006.
[29] N. Roshandel Tavana and V. Dinavahi, "A general framework for FPGA-based real-time emulation of electrical machines for HIL applications," *IEEE Trans. Ind. Electron.*, vol. 62, no. 4, pp. 2041–2053, Apr. 2015.
[30] Y. Chen and V. Dinavahi, "Digital hardware emulation of universal machine and universal line models for real-time electromagnetic transient simulation," *IEEE Trans. Ind. Electron.*, vol. 59, no. 2, pp. 1300–1309, Feb. 2012.
[31] Y. Chen and V. Dinavahi, "An iterative real-time nonlinear electromagnetic transient solver on FPGA," *IEEE Trans. Ind. Electron.*, vol. 58, no. 6, pp. 2547–2555, Jun. 2011.
[32] *7 Series FPGAs Overview*, Xilinx Inc., San Jose, CA, USA, Oct. 2014.

Nariman Roshandel Tavana (S'08) was born in Rasht, Iran, in 1983. He received the B.Sc. degree in electrical engineering from the University of Guilan, Guilan, Iran, in 2006, and the M.Sc. (Hons.) degree in electrical power engineering (power electronics and electric machines) from the Iran University of Science and Technology, Tehran, Iran, in 2009. He is currently pursuing the Ph.D. degree with the Department of Electrical and Computer Engineering, University of Alberta, Edmonton, AB, Canada.

His current research interests include field-programmable gate array-based real-time simulation, design and modeling of electrical machines, finite-element analysis of electromagnetic devices, and motor drives.

Venkata Dinavahi (S'94–M'00–SM'08) received the Ph.D. degree from the University of Toronto, Toronto, ON, Canada, in 2000.

He is currently a Professor with the Department of Electrical and Computer Engineering, University of Alberta, Edmonton, AB, Canada. His current research interests include real-time simulation of power systems, large-scale system simulation, and parallel and distributed computing.